Journal of
Electronic Imaging

SPIEDigitalLibrary.org/jei

Adaptive Charbonnier superresolution method with robust edge preservation capabilities

Baraka J. Maiseli
Qiang Liu
Ogada A. Elisha
Huijun Gao

SPIE

IS&T
imaging.org

Adaptive Charbonnier superresolution method with robust edge preservation capabilities

Baraka J. Maiseli
Harbin Institute of Technology
Research Institute of Intelligent Control and Systems
Harbin 150001, China
and
University of Dar es Salaam
College of Information and Communication Technologies
Department of Electronics and Telecommunication Engineering
P.O. Box 35194
Dar es Salaam, Tanzania
E-mail: barakamaiseli@yahoo.com

Qiang Liu
Harbin Institute of Technology
Research Institute of Intelligent Control and Systems
Harbin 150001, China

Ogada A. Elisha
Harbin Institute of Technology
Department of Mathematics
Harbin 150001, China
and
Egerton University
Department of Mathematics
P.O. Box 536
Egerton, Kenya

Huijun Gao
Harbin Institute of Technology
Research Institute of Intelligent Control and Systems
Harbin 150001, China

Abstract. *Superresolution (SR) is known to be an ill-posed inverse problem, which may be solved using some regularization techniques. We have proposed an adaptive regularization method, based on a Charbonnier nonlinear diffusion model to solve an SR problem. The proposed model is flexible because of its automatic capability to reap the strengths of either linear isotropic diffusion, Charbonnier model, or semi-Charbonnier model, depending on the local features of the image. On the contrary, the models proposed from other research works are fixed and hence less feature dependent. This makes such models insensitive to local structures of the images, thereby producing poor reconstruction results. Empirical results obtained from experiments, and presented here, show that the proposed method produces superresolved images which are more natural and contain well-preserved and clearly distinguishable image structures, such as edges. In comparison with other methods, the proposed method demonstrates higher performance in terms of the quality of images it generates.* *[DOI: 10.1117/1.JEI.22.4.043027]*

Paper 13515 received Sep. 9, 2013; revised manuscript received Oct. 20, 2013; accepted for publication Nov. 13, 2013; published online Dec. 16, 2013.

0091-3286/2013/$25.00

1 Introduction

1.1 *Background of the Superresolution Technology*

In most industrial and domestic imaging applications, high quality images with high resolution (HR) are usually required. There are two basic reasons for this requirement. First, it is natural for end users to appreciably desire images with better visual appeal than poor ones. Second, HR images are required in various disciplines of image processing. For example, doctors require HR medical images, such as images to help in locating brain tumors and to provide appropriate treatments to patients. For these reasons, several technologies have been explored to meet these demands. One of these technologies is called super resolution (SR).[1–4] This technology is used to generate HR images from at least one set of low resolution (LR) images. There are two classifications of SR, namely, single-frame based SR[3,5] and multiple-frame based SR.[6] Single-frame SR methods use a single LR image to reconstruct a HR image, whereas multiple-frame SR methods involve sequences of LR images to reconstruct an HR image. In this article, we focus on multiple-frame SR methods.

For the sake of comprehensively providing understanding of an SR problem, we shall adopt the observation model in Ref. 1 to demonstrate a relationship between LR and HR images. The observation model, hereinafter referred to as OM, provides descriptions of all possible degradation processes; an ideal HR image is likely to go toward generating corresponding LR images. Let us consider an OM shown in Fig. 1, in which the variables R_k, H_k, and T_k, respectively, represent the warping, blurring, and decimation operators, and e_k, u, and y_k, respectively, stand for the additive noise, HR image, and observed LR image sequence. According to the figure, the fundamental parameters which result into degradation of u to generate y_k are R_k, H_k, and T_k. The quantity e_k is assumed to be uncorrelated and to have uniform variance in all observed sequences of LR images. The given OM describes u being thrown into a degradation process, where it undergoes warping in block A, blurring in block B, decimation in block C, and noising in block D. Using the OM presented in Fig. 1, we can mathematically model the SR reconstruction process by an equation

$$y_k = R_k H_k T_k u + e_k, \tag{1}$$

where the variables in Eq. (1) are defined in the OM. The optimal solution of u can be found by minimizing the ℓ_2-norm of e_k in Eq. (1). The formulation

$$W(u) = \frac{1}{2}\sum_{k=1}^{N} \| y_k - R_k H_k T_k u \|_2^2, \tag{2}$$

where $W(u)$ represents the error norm sum of e_k that shows a function we desire to minimize. The convexity of $W(u)$ in Eq. (2) ensures its minimum at a point where its first derivative is zero. Thus, differentiating $W(u)$ with respect to u, we get

$$\nabla W(u) = \sum_{k=1}^{N} R_k^T H_k^T T_k^T (R_k H_k T_k u - y_k). \tag{3}$$

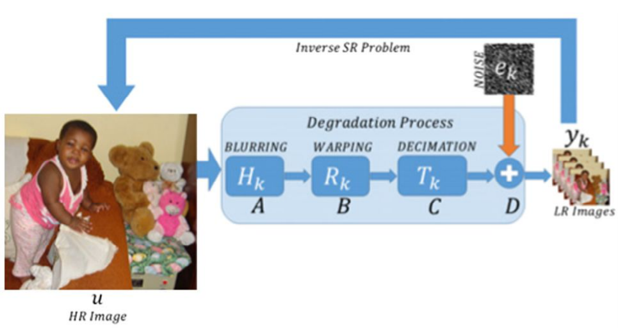

Fig. 1 Superresolution (SR) observation model.

Equating Eq. (3) to zero and embedding the resulting equation into a dynamical system, yields the evolution equation given by

$$\partial_t u = \sum_{k=1}^{N} R_k^T H_k^T T_k^T (y_k - R_k H_k T_k u). \tag{4}$$

Equation (4) may be rewritten in a more compact form as

$$\partial_t u = \sum_{k=1}^{N} (b_k^T y_k - b_k^T b_k u), \tag{5}$$

where b_k is a transformation matrix with operators R_k, H_k, and T_k defined in the OM.

The SR problem has increasingly seized the attention of researchers in the world of digital image processing. Consequently, different methods have been proposed to address it. The authors in Ref. 7, for instance, proposed a robust superresolution (RSR) method for image reconstruction. Their approach combines a median estimator in the iterative process, which, as a result, makes the method more robust against outliers. Empirical results show that this method outperforms the iterative back projection method proposed in Ref. 8, which does not provide an effective capability for outlier detection in a noisy data. Despite its robustness, the RSR has some weaknesses, as pointed out in Ref. 9. In their work, Farsiu et al.[9] provide a proof that under particular situations, the median estimator proposed by Zomet et al.[7] is zero for all iterations. When this occurs, the final generated HR image becomes equal to the initial guess and the method then collapses.

SR falls within a class of well-known ill-posed inverse problems.[10–12] This means that in the underdetermined state, there exists infinitely many solutions satisfying Eq. (1). Furthermore, square and overdetermined cases result in solutions which are unstable and unreliable, implying that the system is ill conditioned. Due to these challenges which the already discussed SR methods have not addressed, regularization approaches have been proposed by some authors as one of the possible solutions to the challenges. As an added advantage, regularization methods improve the convergence rates and also provide solutions with minimal artifacts or unnecessary new features.

Perhaps one of the most widely used regularization method is the total variation (TV), which was originally proposed by Rudin–Osher–Fatemi (ROF) in Refs. 13–15. In the context of images, the TV regularization approach is based on the fact that the TV of an image with excessive and possibly spurious contents, such as noise and unusual artifacts, is high. Therefore, the summation of the absolute of the image gradient under such circumstances is high. According to the ROF approach, if recovery of the original signal is required, one should minimize the TV of the signal subjected to it. In this way, crucial image features, such as edges and contours, are preserved while unwanted details are de-emphasized. Although this method offers a number of merits, it also has some drawbacks. One, the method has a tendency to produce false edges in images severely degraded by noise. Two, given that the method is more efficient in preserving edges of uniform and small curvature, it may excessively smoothen and possibly destroy small scale features having more pronounced curvature edges. Three, the TV regularization approach may result into loss of contrast and geometry of the final output images.[16]

Another regularization method, which is based on diffusion processes, was proposed by Perona and Malik.[17] In this work, the authors propose a diffusion coefficient which can spatially control the rate of diffusion in the image regions. Therefore, the method does noise removal while simultaneously preserving important image details. Despite its merits, there are certain important weaknesses of this method. For instance, the flux function proposed by the authors is nonmonotone and not entirely convex [see Eqs. (10) and (11)]. This raises the issue of well-posedness which remains an open question in mathematics for such class of functions. Theoretically, uncontrolled non-monotone and non-convex functions are unstable and may produce infinitely many solutions with respect to the initial image.[18–21] An alternative flux function which is monotone and convex at all times was proposed by Charbonnier et al.[22] Practical implementations of this method show better results than the Perona-Malik approach which, additionally, suffers speckle effects. Under certain circumstances, however, the Charbonnier method has a tendency of introducing new features to the final solution.

Motivated by these challenges, we propose a method which can adaptively regularize an image on the basis of its local structural characteristics. The proposed method automatically adjusts its formulation to exploit the advantages of the normal heat diffusion process, Perona-Malik, Charbonnier, and other in-between models. The approach used in the new method is similar to the one proposed by Guo et al.[23] The adaptative mechanism of the method proposed by authors in Ref. 23, however, does not exploit the full potentials of the Charbonnier method and other related in-between models. Experiments performed on real images show that our method produces better results in comparison to the state-of-the-art works.

1.2 *Overview of Diffusion Processes*

Because of the dependence of the proposed SR model on the diffusion processes, it is useful to discuss some of the issues related to these processes. In this subsection, we first provide a general definition of diffusion and its mode of operation. Second, various methods which use diffusion process techniques in the regularization of images are discussed. The common theoretical and practical problems in the operation of these methods are also introduced. Furthermore, an alternative method, called the Charbonnier, which addresses some of the challenges in the traditional diffusion-based methods, is briefly discussed. The basis of the Charbonnier method is used to form a building block for our method.

Generally, the term diffusion can be described as a physical process that involves movement of particles from regions of high concentration to regions of low concentration without creating or destroying mass.[24] This migration of particles continues until equilibrium conditions of the system undergoing the diffusion process is established. The Fick's first law:

$$j = -D \cdot \nabla u, \tag{6}$$

where D is the diffusivity coefficient and ∇u is the driving force causing flux, which relates the diffusive flux j to the intensity u when steady state conditions are assumed. If j and ∇u are parallel then diffusion is called isotropic, otherwise it is called anisotropic.

The idea that mass can neither be created nor destroyed during diffusion can well be modelled by the continuity equation:

$$\partial_t u = -\mathrm{div}\, j, \tag{7}$$

where t denotes the time. If Eq. (6) is plugged into Eq. (7), a general diffusion equation

$$\partial_t u = \mathrm{div}(D \cdot \nabla u) \tag{8}$$

is formed. Several physical transport processes utilize this diffusion equation. In heat transfer, for example, it is called the heat equation.

In the field of image processing, the variable concentration used in diffusion is related to the intensity at a given pixel location of an image. Thus, diffusion with respect to images is defined as the transportation of intensity from regions with higher values to regions with lower values until an image attains stable conditions. Indeed, this is a smoothing or filtering process. Recalling the diffusion Eq. (8), if D is constant over the entire image domain the diffusion is called homogeneous. However, if D is space dependent, the diffusion is called inhomogeneous. The diffusion tensor D is usually a function of the gradient of the evolving image u and this feedback mechanism makes the whole diffusion process nonlinear.

In the nonlinear isotropic diffusion process, an effective smoothing is provided over a long time while maintaining sharp edges. This can easily be established when the diffusivity g is made to depend on the gradient of the actual evolving image $u(x,t)$. Originally, the idea of nonlinear diffusion was proposed by Perona–Malik (PM),[17] in which the relationship between the evolving image u and g is given by

$$\partial_t u = \mathrm{div}(g(|\nabla u|^2) \cdot \nabla u), \tag{9}$$

with g defined as

$$g(|\nabla u|) = \frac{1}{1 + \left(\frac{|\nabla u|}{\lambda}\right)^2}, \qquad \lambda > 0. \tag{10}$$

In their research work, Perona and Malik demonstrate impressive visual results. It was shown in Ref. 17 that the PM scheme outperforms most edge detectors, including the traditional Canny edge detector,[25,26] even when nonmaximum suppression and hysteresis thresholding are not applied. One of the weaknesses of the PM regularization model, however, is that its final solution is at a higher risk of suffering from staircasing effects.[27–29] Moreover, the potential function $\psi(s)$, where $s = |\nabla u|$, proposed by Perona and Malik in the equation

$$\psi(s) = \frac{\lambda^2}{2} \log\left[1 + \left(\frac{s}{\lambda}\right)^2\right] \tag{11}$$

is convex only for $|s| \leq \lambda$, and this constraint poses a challenge when selecting appropriate values of λ to generate optimal solutions. The characteristics of the nonconvex variational problems, such as the PM scheme, have been numerically analyzed in Refs. 30 and 31. The authors provide proofs of the possibilities of the minimizing sequences of the functional to develop gradient oscillations. Consequently, the oscillations can decrease the magnitude of the functional.

In Ref. 22, Charbonnier and others proposed an alternative potential function

$$\psi(s) = \sqrt{\lambda^4 + \lambda^2 s^2} - \lambda^2, \tag{12}$$

of which, when the corresponding energy functional is minimized, produces diffusivity

$$g(s^2) = \frac{1}{\sqrt{1 + (\frac{s}{\lambda})^2}}. \tag{13}$$

Contrary to the PM scheme, this energy functional is convex for all s regardless of the chosen value of λ. In addition, visual results are better compared to the PM regularization approach. The weakness of the Charbonnier approach is that it regularizes the image independently of the image structures. Also, it suffers from speckles just like the PM approach.

We have discussed important concepts of the SR technology in this section. In particular, the methods used to solve a SR problem and their weaknesses have been thoroughly explored. We have also introduced some of the applications of the technology in real life. Furthermore, a motivation for doing this research is given. All the foregoing concepts are used as the building blocks for the forthcoming sections. Now, the remainder of the article is organized as follows. In Sec. 2, the proposed feature-dependent method is given. In Sec. 3, the numerical scheme used to implement the proposed method is discussed. This section also includes some explanations on the convergence speeds of our method. The experimental results are introduced and discussed in Sec. 4 and the article is concluded in Sec. 5.

2 α-Charb Adaptive SR Method

In this section, an α-charb adaptive SR method is proposed. The fundamental characteristic of the method is that the regularization part automatically switches in response to the image structures. Additionally, the range of the values of the parameter α controlling model selection is automatically determined within the program. Therefore, we propose an SR model which combines an evolution equation from the variational problem given by

$$\inf_u \left\{ Z(u) = \frac{1}{2N} \sum_{k=1}^{N} \| y_k - b_k u \|_2^2 + \frac{\gamma_2}{2} \| u - u_0 \|_2^2 \right\}, \tag{14}$$

and non-variational regularization elliptic problem given by

$$0 = \operatorname{div}\left(\frac{\nabla u}{\left(1 + \left[\frac{|\nabla u|}{K}\right]^{\alpha(x)}\right)^{\frac{1}{\alpha(x)+\epsilon}}} \right). \tag{15}$$

From Eq. (14), we obtain the Euler–Lagrange equation

$$0 = \frac{1}{N} \sum_{k=1}^{N} (b_k^T b_k u - b_k^T y_k) - \gamma_2 (u - u_0). \tag{16}$$

Combining Eqs. (15) and (16) and embedding into a dynamical system, we obtain the proposed adaptive SR evolution equation:

$$\begin{aligned} \partial_t u = {} & \sum_{k=1}^{N} (b_k^T b_k u - b_k^T y_k) + \gamma_1 N \nabla \\ & \cdot \Upsilon_\epsilon(|\nabla u|, \nabla u, \alpha(x), K) - \gamma_2 N (u - u_0), \end{aligned} \tag{17}$$

from which u can be estimated, where

$$\Upsilon_\epsilon(\cdot) = \frac{\nabla u}{\left(1 + \left[\frac{|\nabla u|}{K}\right]^{\alpha(x)}\right)^{\frac{1}{\alpha(x)+\epsilon}}}$$

where γ_1 is a regularization parameter and $\gamma_2 (u - u_0)$ is a fidelity forcing term.

In Eq. (17), $0 \le \alpha(x) \le 2$. It is clear from the formulation in Eq. (17) that the proposed model provides an automatic interplay among different models for the given values of $\alpha(x)$. For instance, when $\alpha(x) = 0$, the formulation is linear isotropic diffusion. Additionally, when $\alpha(x) = 1$, we get an approximation of the Charbonnier model, and the ideal Charbonnier formulation is achieved when $\alpha(x) = 2$.

In order to make the whole process self-controlled, $\alpha(x)$ is automatically determined in the regularization process, we define[23]

$$\alpha(x) := 2 - \frac{2}{1 + \kappa |\nabla G_\sigma * u|^2}, \tag{18}$$

where

$$G_\sigma(x) := \frac{1}{(4\pi\sigma)^{N/2}} \exp(-|x|^2 / 4\sigma).$$

Our final code implementation of the proposed model is designed in such a way that it automatically selects the values of the parameter $\alpha(x)$ on the basis of the local image structures. The edge detector of the proposed method is given by the equation

$$E(x, u) = \frac{1}{\left(1 + \left[\frac{|\nabla u|}{K}\right]^{\alpha(x)}\right)^{\frac{1}{\alpha(x)+\epsilon}}}. \tag{19}$$

As will be demonstrated in Sec. 3, this edge detector generates more pronounced edges than the edge detectors proposed in Refs. 17 and 23.

Finally, we show the decomposition of Eq. (17) into the tangent and normal directions to the isophote lines. Consider an arbitrary pixel point (x, y) in the image, where $|\nabla u(x,y)| \neq 0$, then we can define vectors $N(x) = \nabla u/|\nabla u|$ and $T(x) = (-u_y, u_x)/|\nabla u|$ such that $T(x)$ is orthogonal to $N(x)$. If u_{TT} and u_{NN} represent the second order derivatives of u in the T and N directions, respectively, and are defined as

$$\begin{aligned} u_{TT} &= T'\nabla^2 uT = \frac{1}{|\nabla u|^2}(u_x^2 u_{yy} + u_y^2 u_{xx} - 2u_x u_y u_{xy}) \\ u_{NN} &= N'\nabla^2 uN = \frac{1}{|\nabla u|^2}(u_x^2 u_{xx} + u_y^2 u_{yy} + 2u_x u_y u_{xy}), \end{aligned} \tag{20}$$

then Eq. (17) can be written as

$$\begin{aligned} \partial_t u = \sum_{k=1}^{N}(b_k^T b_k u - b_k^T y_k) + \gamma_1 N\left(\frac{1}{\left(1+\left[\frac{|\nabla u|}{K}\right]^{\alpha(x)}\right)^{\frac{1}{\alpha(x)+\epsilon}}}\right)u_{TT} \\ + \gamma_1 N\left(\frac{\left[\frac{|\nabla u|}{K}\right]^{\alpha(x)}}{\left(1+\left[\frac{|\nabla u|}{K}\right]^{\alpha(x)}\right)^{\frac{1}{\alpha(x)+\epsilon}+1}}\right)u_{NN} - \gamma_2 N(u-u_0). \end{aligned} \tag{21}$$

One can easily see that the formulation in Eq. (21) contains both the tangential and normal diffusion components, u_{TT} and u_{NN}, respectively. The two components couple up in the evolution equation to orchestrate a regularization process that is productively contour sensitive. That is, edges and important structures of an image are well preserved. Figure 2 gives an illustration of the existence of u_{NN} and u_{TT} components in a curve representing an image structure. If we may recall, one of the challenges in a TV model is the presence of only a u_{TT} component in its formulation.

A complete flow chart describing the adaptive α-Charb SR method is shown in Fig. 3. The practical analysis of our method revealed that when a median filter was integrated into the proposed model, as it can be seen in the flow chart, there was a significant improvement of the quality of the final superresolved images. More specifically, speckles from final images were removed. This can be explained from the fact

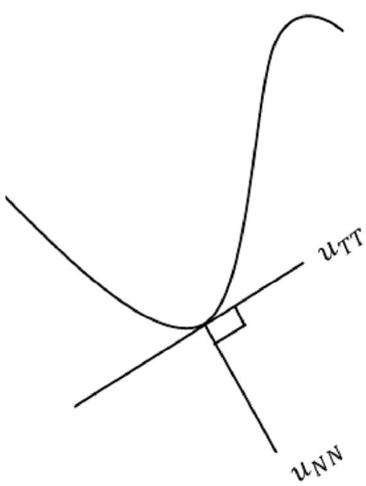

Fig. 2 Normal (u_{NN}) and tangent (u_{TT}) components to an image.

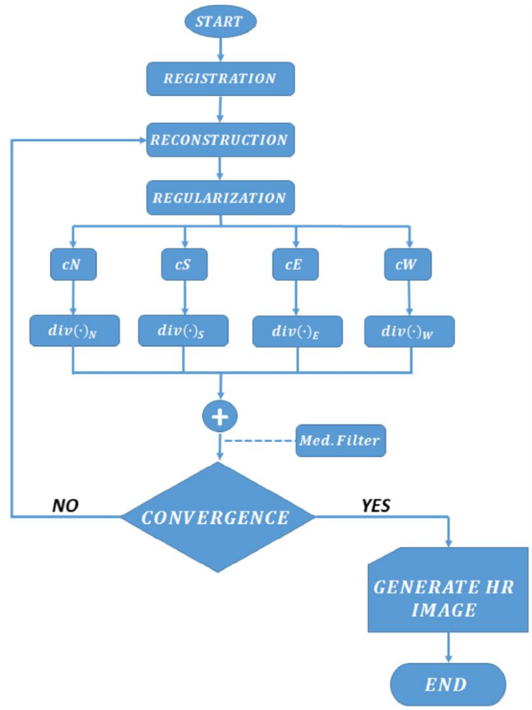

Fig. 3 Flow chart of the α-Charb algorithm.

that median filters are robust against outliers.[32–34] Note that the median filter has a tendency of introducing blurring effects on an image, and for this reason, we chose the minimum kernel size of dimension $[3 \times 3]$ as a way to reduce the effects. Other kernel sizes produced blurred results for the nature of images used and thus could not serve our purpose. It is important to add that the minimum kernel size of 3 proposed may be suitable for all natural images where the noise level is low. The readjustment of the filter kernel is presumably needed for the input images severely degraded by noise. In Fig. 4, we demonstrate the effect of introducing a median filter into our method. From the figure, one can easily see that the visual result of the superresolved Lena image when a median filter is integrated into the α-Charb method is better. The measured peak signal-to-noise ratio (PSNR) value in Fig. 4(a) is 18.0276 while that in Fig. 4(b) (α-Charb method without median filter) is 16.1073.

3 Numerical Scheme Implementation and Analysis

The discrete numerical scheme implementation of the regularization part of our method is shown in Fig. 5. From the

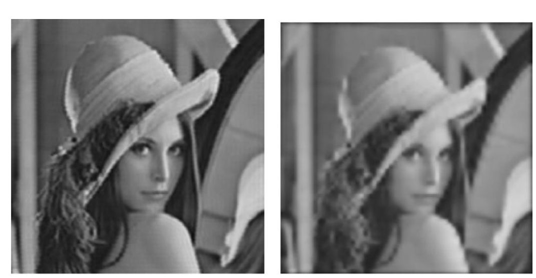

(a) (b)

Fig. 4 Effects of the median filter on the α-Charb method; (a) median filter included, (b) median filter not included.

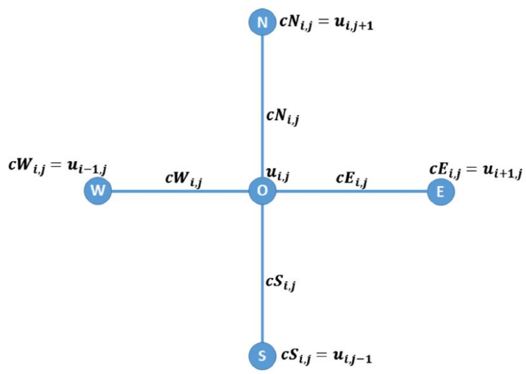

Fig. 5 The discrete numerical scheme.

figure, cN, cS, cW, and cE represent the grid conduction directions. This scheme has been proposed from literature as one of the best approaches to solve nonlinear discrete numerical problems.[35] The problem we are solving in this article falls under the examples of such a class of problems.

We used an explicit scheme to implement our algorithm. This is a scheme in which the calculation of the dependent variables can be done using the already known quantities. There were three major reasons which triggered our interest to use this scheme. First, explicit schemes are relatively easier to implement in the program. Second, the computational load of the explicit schemes is low because of fewer calculation steps required to determine every subsequent space solution. Last, given the fact that this category of schemes is unstable when larger time steps are chosen in the iteration process, in our model, it was, therefore, necessary that our iteration step be made to conform to the Courant–Friedrichs–Lewy (CFL) condition for such schemes.[36] The CFL condition for stability of the explicit scheme demands that $t \leq 0.25$, where t represents the interval between consecutive iterations. We used $t = 0.15$, which satisfies the condition, thereby making the proposed model stable. It is under these circumstances that the α-Charb method demonstrates higher convergence rates and indeed better results in comparison to its competitors. In Table 2, we can observe that the execution speed of the α-Charb method is considerably higher than the ℓ_1-SAR, TV-SR, and ℓ_1-SR methods. Additionally, our algorithm takes a fewer number of iterations in relation to other methods for the reasons already mentioned.

Now, consider the numerical scheme presented in Fig. 5. We would like to show how we used this scheme to implement our method. Let dN, dS, dE, and dW represent the image gradients in the North, South, East, and West directions in the scheme. Then, the discrete versions of these components are

$$dN = u_{i,j+1} - u_{i,j},$$

$$dE = u_{i+1,j} - u_{i,j},$$

$$dS = u_{i,j-1} - u_{i,j},$$

and

$$dW = u_{i-1,j} - u_{i,j},$$

and the corresponding conduction components cN, cS, cE, and cW are

$$cN = \frac{1}{\left(1 + \left[\frac{|dN|}{K}\right]^{\alpha(x)}\right)^{\frac{1}{\alpha(x)+\epsilon}}}$$

$$cS = \frac{1}{\left(1 + \left[\frac{|dS|}{K}\right]^{\alpha(x)}\right)^{\frac{1}{\alpha(x)+\epsilon}}}$$

$$cE = \frac{1}{\left(1 + \left[\frac{|dE|}{K}\right]^{\alpha(x)}\right)^{\frac{1}{\alpha(x)+\epsilon}}}$$

and

$$cW = \frac{1}{\left(1 + \left[\frac{|dW|}{K}\right]^{\alpha(x)}\right)^{\frac{1}{\alpha(x)+\epsilon}}}$$

If we let DVG be the divergence, then

$$\text{DVG} = dN \times cN + dS \times cS + dE \times cE + dW \times cW.$$

The whole α-Charb algorithm was implemented in the MATLAB R2013b platform.

4 Experimental Results and Discussion

We performed experiments to compare our method with the classical methods ℓ_1-SAR, TV-SR, and ℓ_1-SR, proposed in Refs. 37–39, respectively. The machine used in all experiments was Compaq610 with Intel(R), Core(TM)2, Duo CPU T5870 at 2.00 GHz, 2 GB installed physical RAM, and running on 64-bit Windows 7 Professional Operating System. For the methods ℓ_1-SAR, TV-SR, and ℓ_1-SR, we used software provided in Ref. 40. In our method, we used the registration method proposed in Ref. 8 as it showed more accurate estimations of the rototranslation motion parameters.

(a) (b) (c) (d) (e) (f)

Fig. 6 High resolution (HR) images of (a) Lena, (b) Pot, (c) House, (d) Bird, (e) Elephant, (f) Falls.

Fig. 7 One of the low resolution (LR) images generated from the corresponding HR Images of (a) Lena, (b) Pot, (c) House, (d) Bird, (e) Elephant, (f) Falls.

In the first experiment, an HR image of Lena of 240×240 in Fig. 6(a) was decomposed into a sequence of LR frames, each 60×60 resolution and simulated motion parameters, as shown in Fig. 7(a). A similar procedure was repeated, but using the images of a Pot, House, Bird, Elephant, and Falls [see Figs. 6(b)–6(f) and Figs. 7(b)–7(f), which represent the HR images and their corresponding LR images, respectively]. Finally, the LR images were passed through the reconstruction methods ℓ_1-SAR, TV-SR, ℓ_1-SR, and α-Charb to generate the HR images. Some of the results of the superresolved images are shown in Figs. 8–11.

In addition, the PSNR (Ref. 41) and the edge structural similarity (ESSIM)[42] of the HR image generated from each of the methods were computed, as Table 1 illustrates. Additionally, we evaluated the performance of the methods using the total number of iterations N, a given method takes to complete execution, and the CPU time (in seconds), as shown in Table 2. In order to provide static values, the mean and standard deviation of the measured data were calculated. From Table 1, one can observe that the average ESSIM of the α-Charb is higher than that from other methods. This suggests that the proposed method offers higher capabilities in edge preservation. Furthermore, the average PSNR of the proposed method is higher than the other methods. This implies that our method generates images with higher signal strengths. A careful observation on the entries of Table 1 further suggests that the proposed model slightly underperforms for the House and Falls images. We think that this is possibly caused by the nature of the images and the method used to capture them. Furthermore, recalling back from Sec. 1, we have mentioned that SR has two components, namely registration, which estimates some motion parameters between pairs of input frames, and reconstruction, in which the α-Charb method resides. If registration is inefficiently done, it may result in unsatisfactory reconstruction. Having said that, it is obvious that the registration method used needs a slight improvement so that the roto-translation motion parameters for small-scale featured images, such as the House and Falls images, can accurately be estimated. Just like all other reconstruction methods, the proposed method may produce promising results in these particular cases when a good registration method is put forward.

In terms of the computational efficiency, Table 2 shows that our method is 87×, 127×, and 134× faster than the

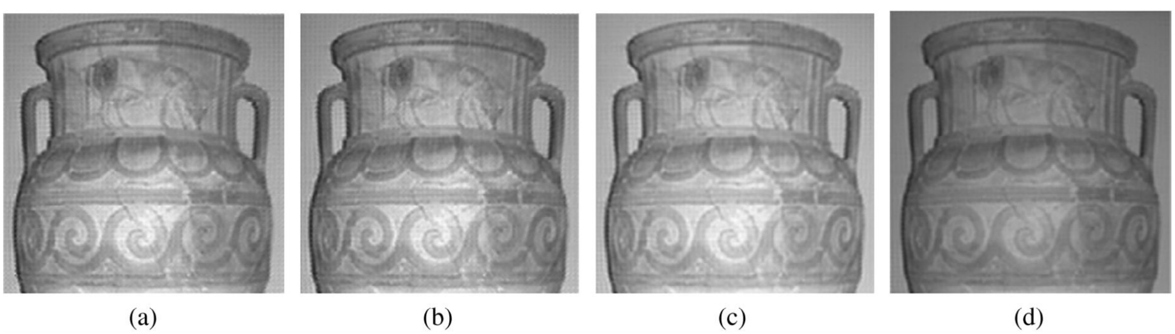

Fig. 8 SR reconstruction using a Pot image; (a) ℓ_1-SR, (b) TV-SR, (c) ℓ_1-SAR SR, (d) α-charb SR.

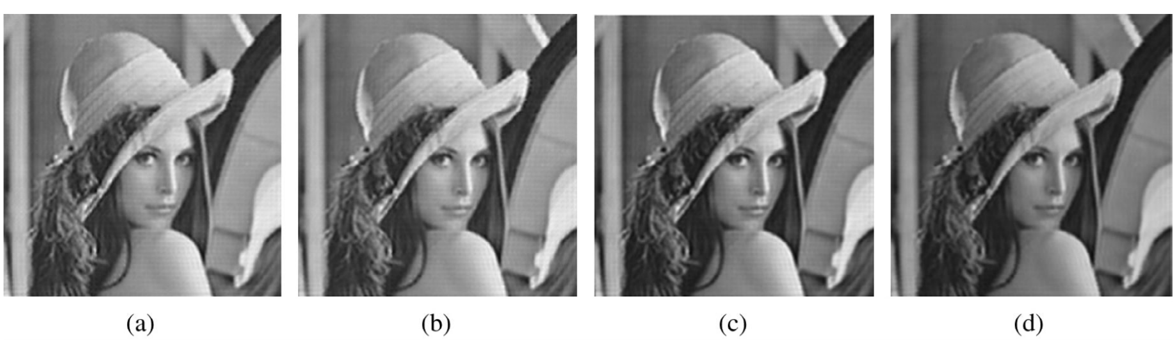

Fig. 9 SR Reconstruction Using a Lena Image; (a) ℓ_1-SR, (b) TV-SR, (c) ℓ_1-SAR SR, (d) α-Charb SR.

(a) (b) (c) (d)

Fig. 10 SR reconstruction using a Bird image; (a) ℓ_1-SR, (b) TV-SR, (c) ℓ_1-SAR SR, (d) α-charb SR.

(a) (b) (c) (d)

Fig. 11 SR reconstruction using an Elephant image; (a) ℓ_1-SR, (b) TV-SR, (c) ℓ_1-SAR SR, (d) α-charb SR.

ℓ_1-SAR, TV-SR, and ℓ_1-SR, respectively. In fact, speed is one of the essential requirements in the implementation of real-time industrial systems, such as fault-tolerant control systems.[43,44] Moreover, using subjective assessment methods, the images in Figs. 8–12 demonstrate that the α-Charb method generates HR images which are sharp and smooth. The results show that the other methods have a tendency to add some new features which were not contained in the original images. Also, the output images in the approaches proposed by other authors are unnecessarily brightened. This makes these images lose their naturalness. Our intuition on the extra features, such as brightness, introduced into the results of the other methods is that, since the methods take a significantly large number of iterations to complete execution (see the performance evaluation Table 2), there is a possibility that the evolving images are repeatedly exposed to over-regularization during the iteration process. As we can see, these methods incorporate in their formulations ℓ_1 and TV regularizing functionals. Therefore, some image features can be washed out in the course of regularization and the situation is worse if the model allows input images to stay long enough before reaching stable conditions. More research is possibly needed to study the operation of these methods for different types of images and conditions.

In Fig. 13, we illustrate the similarity between the original image and the images generated when different SR algorithms are applied. In each of the plots, we converted a corresponding two-dimensional image into a line profile through fixing a particular column and making a line plot across all rows. Although this strategy does not exploit all similarity possibilities, it roughly shows how close an image is from the original under the given conditions. However, we tried to sample different columns and make plots for all rows in a given sampled column, and the results did not vary widely. Figure 13 depicts one of the sampled columns. The plots presented in this figure are generated using an Elephant image shown in Fig. 11. One can easily see from the plots that the similarity curve of our method closely traces the original curve, thus signaling a higher degree of similarity between the original image and the generated image in comparison to other methods. For example, the extracted portion D of the lower right corner plot demonstrates a good match of the two curves with respect to the portions A, B, and C from the other plots of the figure.

(a) (b) (c) (d)

Fig. 12 SR reconstruction using a House image; (a) ℓ_1-SR, (b) TV-SR, (c) ℓ_1-SAR SR, (d) α-charb SR.

Table 1 Peak signal-to-noise ratio (PSNR) and edge structural similarity (ESSIM) comparison results.

	Method							
	ℓ_1-SAR		TV-SR		ℓ_1-SR		α-Charb	
Image	PSNR	ESSIM	PSNR	ESSIM	PSNR	ESSIM	PSNR	ESSIM
Lena	16.92	0.85	17.31	0.80	16.67	0.80	18.03	0.89
House	19.47	0.85	19.58	0.85	19.58	0.83	19.00	0.69
Bird	16.12	0.76	16.58	0.70	16.27	0.70	17.57	0.89
Pot	14.33	0.73	14.21	0.77	14.29	0.79	22.95	0.93
Elephant	19.28	0.82	19.28	0.71	18.92	0.79	22.18	0.91
Falls	18.11	0.82	18.08	0.80	18.31	0.74	18.79	0.70
Mean	17.37	0.81	17.50	0.77	17.34	0.77	19.75	0.84
STD	1.98	0.05	1.98	0.06	1.97	0.05	2.25	0.11
Ranking	3	2	2	4	4	4	1	1

Table 2 Performance evaluation results.

	Method							
	ℓ_1-SAR		TV-SR		ℓ_1-SR		α-Charb	
Image	N	CPU Time (τ)	N	CPU Time (τ)	N	CPU Time (τ)	N	CPU Time (τ)
Lena	37	784.89	83	1860.72	86	1650.37	16	12.30
House	54	1149.40	48	908.40	63	1178.40	18	13.39
Bird	38	804.30	98	2001.84	107	2159.72	18	13.06
Pot	80	1752.10	91	1921.03	100	2106.74	16	12.45
Elephant	52	989.81	94	1939.86	87	2013.40	17	12.62
Falls	56	1094.99	56	1010.99	59	1073.48	16	12.13
Mean	53	1095.90	78	1607.10	84	1697.00	17	12.66
Speed		$\tau/87$		$\tau/127$		$\tau/134$		τ

It has been reported in Refs. 23, 45, and 46 that the PSNR quantity does not provide a satisfactory measure of the quality of edges in an image. The authors in Ref. 45 propose a method given by

$$\widetilde{\mathrm{PSNR}} = 10\log_{10}\left(\frac{\mathrm{MN}|\max(u_0) - \min(u_0)|}{\|u - u_0\|_2^2}\right), \tag{22}$$

which can effectively measure the similarity of the edges in the images. This method outperforms several other edge similarity comparison methods and, for this fact, we combine it with the proposed edge detector in (19) to form the relation

$$\mathrm{PSNR}_X = \widetilde{\mathrm{PSNR}}[E(x,u), E(x,u_0)]. \tag{23}$$

In Table 3, the numerical values of PSNR_X for the SR results show that our method is superior over others in the aspect of edge similarity.

We also realized that it was worthwhile to conduct another experiment which could show the strength of the α-Charb method in the aspect of recovering, preserving, and enhancing edges. We used a simple low-textured image [see Fig. 14(a)] for quick analysis of the performances of the edge detectors. This experiment was done using the proposed

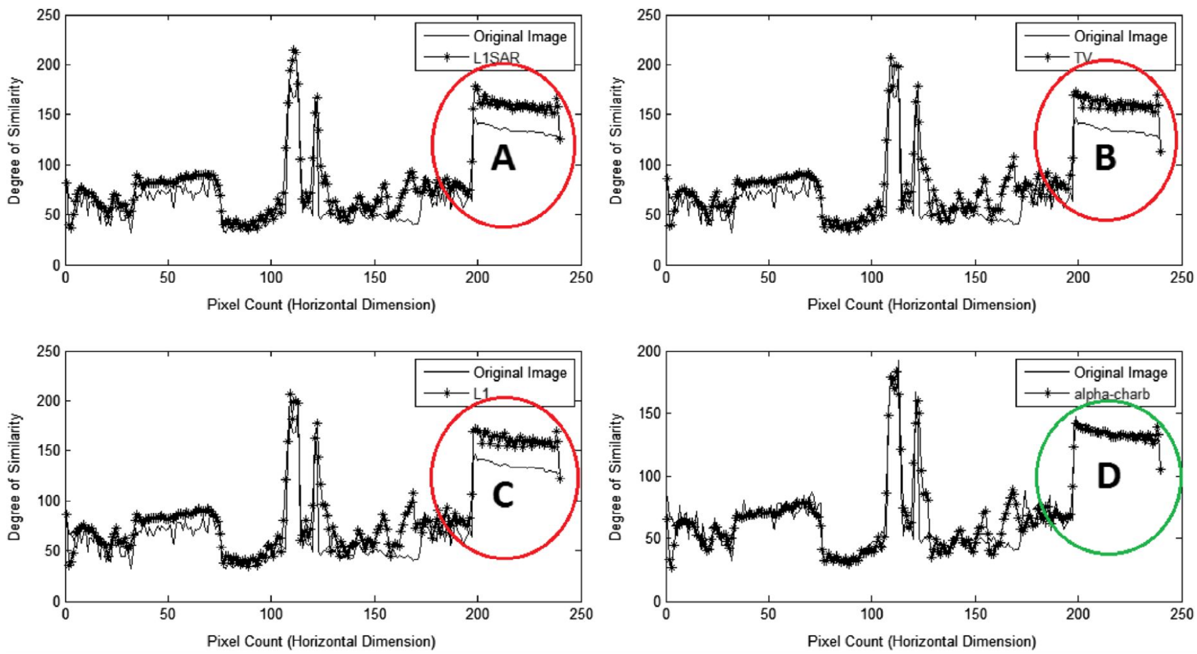

Fig. 13 Similarity plots for different SR methods.

Table 3 Results for PSNR X values of different methods.

	Method			
Image	ℓ_1**-SAR**	**TV-SR**	ℓ_1**-SR**	α**-Charb**
Elephant	19.12	18.88	18.83	22.43
Pot	13.96	14.81	12.87	18.94
Bird	15.26	15.70	15.45	16.78
Lena	15.46	16.02	15.46	16.58
Mean	15.95	16.35	15.65	18.68
Ranking	3	2	4	1

edge detector in Eq. (19) and the edge detectors proposed by Guo and Perona-Malik. In Fig. 14, we can see that the edges and contours produced by the proposed edge detector, $E(x, u)$, are enhanced and clearly distinguishable. The results from other methods are relatively faint and less enhanced.

5 Conclusion

A regularization method for solving an SR problem has been proposed in this article. The method is adaptive because it has capabilities to automatically adjust itself on the basis of the local image structures. The proposed adaptive parameter $\alpha(x)$ is a function of the local image structure, and it is determined without any manual manipulation. Experiments done from a couple of datasets demonstrate that the proposed method is faster and more efficient than the other methods. This implies that the method may be applied in real-time hardware platforms. Additionally, superresolved images generated by the α-Charb method are sharp, more natural and have edges and contours well preserved. From the tables' results, it may be realized that the signal strength of the output images in our method is higher with respect to

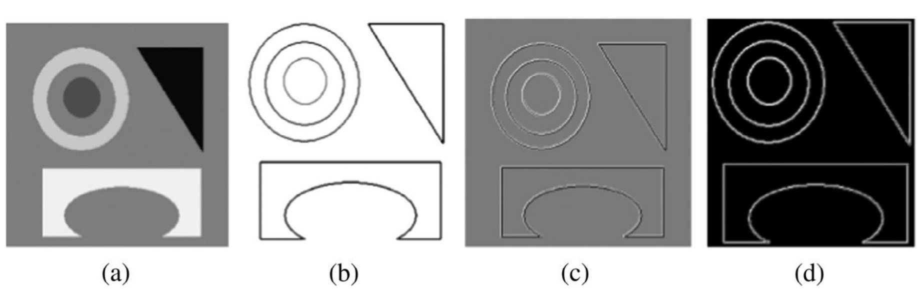

Fig. 14 Edge maps for edge detectors of various methods (a) original image, (b) Perona–Malik (PM) edge detector (Ref. 17), (c) Guo edge detector (Ref. 23), (d) proposed edge detector.

others. This means that the method may be suitable in digital signal processing applications. There are certain imaging applications where one is interested in signal content during processing and analysis of the image.

References

1. S. C. Park, M. K. Park, and M. G. Kang, "Super-resolution image reconstruction: a technical overview," *IEEE Signal Process. Mag.* **20**(3), 21–36 (2003).
2. S. Borman and R. L. Stevenson, "Super-resolution from image sequences—a review," in *Proc. 1998 Midwest Symposium Circuits and Systems*, pp. 374–378, IEEE (1998).
3. D. Glasner, S. Bagon, and M. Irani, "Super-resolution from a single image," in *IEEE 12th Int. Conf. Computer Vision*, pp. 349–356, IEEE (2009).
4. J. Van Ouwerkerk, "Image super-resolution survey," *Image and Vision Computing* **24**(10), 1039–1052 (2006).
5. W. T. Freeman, T. R. Jones, and E. C. Pasztor, "Example-based super-resolution," *IEEE Comput. Graph. Appl.* **22**(2), 56–65 (2002).
6. S. Farsiu et al., "Advances and challenges in super-resolution," *Int. J. Imaging Syst. Technol.* **14**(2), 47–57 (2004).
7. A. Zomet, A. Rav-Acha, and S. Peleg, "Robust super-resolution," in *Proc. IEEE Comput. Soc. Conf. Computer Vision and Pattern Recognition*, Vol. 1, pp. I-645, IEEE (2001).
8. M. Irani and S. Peleg, "Improving resolution by image registration," *CVGIP Graph. Models Image Process.* **53**(3), 231–239 (1991).
9. S. Farsiu et al., "Fast and robust multiframe super resolution," *IEEE Trans. Image Process.* **13**(10), 1327–1344 (2004).
10. I. R. Bleyer and R. Ramlau, "A double regularization approach for inverse problems with noisy data and inexact operator," *Inverse Problems* **29**(2), 025004 (2013).
11. H. Song et al., "Adaptive regularization-based space-time super-resolution reconstruction," *Signal Process. Image Commun.* **28**(7), 763–778 (2013).
12. S. Yan-Xin and C. Yong-Mei, "Super-resolution image reconstruction with adaptive regularization parameter," *Int. J. Appl. Math. Statist.* **39**(9), 227–235 (2013).
13. L. I. Rudin, S. Osher, and E. Fatemi, "Nonlinear total variation based noise removal algorithms," *Phys. D Nonlinear Phenomena* **60**(1), 259–268 (1992).
14. T. Goldstein and S. Osher, "The split Bregman method for l1-regularized problems," *SIAM J. Imaging Sci.* **2**(2), 323–343 (2009).
15. P. Getreuer, "Rudin-osher-fatemi total variation denoising using split bregman," *Image Process. Online* **10** (2012).
16. T. Chan et al., "Recent developments in total variation image restoration," in *Math. Models Comput. Vision*, Vol. 17, pp. 17–31, Springer Verlag (2005).
17. P. Perona and J. Malik, "Scale-space and edge detection using anisotropic diffusion," *IEEE Trans. Pattern Anal. Mach. Intell.* **12**(7), 629–639 (1990).
18. S. Kichenassamy, "The Perona–Malik paradox," *SIAM J. Appl. Math.* **57**(5), 1328–1342 (1997).
19. P. Perona, T. Shiota, and J. Malik, "Anisotropic diffusion," in *Geometry-Driven Diffusion in Computer Vision*, pp. 73–92, Springer, Netherlands (1994).
20. S. Kichenassamy, "Nonlinear diffusions and hyperbolic smoothing for edge enhancement," in *ICAOS'96*, pp. 119–124, Springer, Berlin Heidelberg (1996).
21. K. Hollig, "Existence of infinitely many solutions for a forward-backward heat equation," *Trans. Am. Math. Soc.* **278**(1), 299–316 (1983).
22. P. Charbonnier et al., "Two deterministic half-quadratic regularization algorithms for computed imaging," in *IEEE Int. Conf. Proc. Image Processing*, Vol. 2, pp. 168–172, IEEE (1994).
23. Z. Guo et al., "Adaptive Perona–Malik model based on the variable exponent for image denoising," *IEEE Trans. Image Process.* **21**(3), 958–967 (2012).
24. J. Weickert, "A review of nonlinear diffusion filtering," in *Scale-Space Theory in Computer Vision*, pp. 1–28, Springer, Berlin Heidelberg (1997).
25. J. Canny, "A computational approach to edge detection," *IEEE Trans. Pattern Anal. Mach. Intell.* **PAMI-8**(6), 679–698 (1986).
26. L. Ding and A. Goshtasby, "On the canny edge detector," *Pattern Recognit.* **34**(3), 721–725 (2001).
27. B. Benhamouda, "Parameter adaptation for nonlinear diffusion in image processing," Master's Thesis, Department of Mathematics, University of Kaiserslautern (1994).
28. J. Fröhlich and J. Weickert, *Image Processing Using a Wavelet Algorithm for Nonlinear Diffusion*, University of Kaiserslautern, Fachbereich Mathematik (1994).
29. M. Nitzberg and T. Shiota, "Nonlinear image filtering with edge and corner enhancement," *IEEE Trans. Pattern Anal. Mach. Intell.* **14**(8), 826–833 (1992).
30. M. Chipot, R. March, and D. Vitulano, "Numerical analysis of oscillations in a nonconvex problem related to image selective smoothing," *J. Computat. Appl. Math.* **136**(1), 123–133 (2001).
31. A. Blake and A. Zisserman, *Visual Reconstruction*, Vol. 2, MIT Press, Cambridge (1987).
32. V. V. Khryashchev et al., "Image denoising using adaptive switching median filter," in *IEEE Int. Conf. Image Processing*, Vol. 1, pp. I-117, IEEE (2005).
33. R. H. Chan, C.-W. Ho, and M. Nikolova, "Salt-and-pepper noise removal by median-type noise detectors and detail-preserving regularization," *IEEE Trans. Image Process.* **14**(10), 1479–1485 (2005).
34. S. Akkoul et al., "A new adaptive switching median filter," *IEEE Signal Process. Lett.* **17**(6), 587–590 (2010).
35. J. F. Epperson, *An Introduction to Numerical Methods and Analysis*, John Wiley & Sons (2013).
36. R. Courant, K. Friedrichs, and H. Lewy, "On the partial difference equations of mathematical physics," *IBM J. Res. Dev.* **11**(2), 215–234 (1967).
37. S. Villena et al., "Bayesian combination of sparse and non sparse priors in image super resolution," *Digital Signal Process.* **23**(2), 530–541 (2012).
38. S. Babacan, R. Molina, and A. K. Katsaggelos, "Variational Bayesian super resolution," *IEEE Trans. Image Process.* **20**(4), 984–999 (2011).
39. S. Villena et al., "Bayesian super-resolution image reconstruction using an l1 prior," in *Proc. 6th Int. Symp. Image and Signal Processing and Analysis*, pp. 152–157, IEEE (2009).
40. R. Molina et al."Superresolution software," http://decsai.ugr.es/pi/superresolution/software.html (29 February 2013).
41. Z. Wang and A. C. Bovik, "Mean squared error: love it or leave it? a new look at signal fidelity measures," *IEEE Signal Process. Mag.* **26**(1), 98–117 (2009).
42. X. Zhang et al., "Edge strength similarity for image quality assessment," *IEEE Trans. Ind. Electron.* **61**(5), 2402–2411 (2013).
43. S. Yin, H. Luo, and S. Ding, "Real-time implementation of fault-tolerant control systems with performance optimization," *IEEE Trans. Ind. Electron.* **61**(5), 2402–2411 (2013).
44. S. Yin et al., "A comparison study of basic data-driven fault diagnosis and process monitoring methods on the benchmark Tennessee Eastman process," *J. Process Control* **22**(9), 1567–1581 (2012).
45. S. Durand, J. Fadili, and M. Nikolova, "Multiplicative noise removal using l1 fidelity on frame coefficients," *J. Math. Imaging Vision* **36**(3), 201–226 (2010).
46. X.-C. Tai, K.-A. Lie, and T. F. Chan, *Image Processing Based on Partial Differential Equations*, Springer (2007).

Baraka J. Maiseli has been an assistant lecturer at the University of Dar es Salaam (UDSM), Tanzania, since 2010. He obtained his bachelor's degree in electronics science and communication, and master's degree in electronics engineering and information technology, both from UDSM. Currently, he is pursuing his PhD studies at the Harbin Institute of Technology, China. His research interests are in superresolution of digital images, segmentation methods in medical images, and digital signal processors (DSPs).

Qiang Liu received his BE degree in automation from the Harbin Institute of Technology (HIT), Harbin, P. R. China, in 2012. Currently, he is doing his master's degree at the Research Institute of Intelligent Control and Systems at HIT. His research interests are in biometric recognition, robotics, superresolution of digital images, segmentation methods in medical images and digital signal processors (DSPs).

Ogada A. Elisha obtained both his BEd science (mathematics major) and MSc applied mathematics in Egerton University, Kenya. He has been an assistant lecturer in the Department of Mathematics at the same university since 2007, and is currently a PhD student in the Department of Mathematics in the School of Science, Harbin Institute of Technology, China. His research interests include numerical methods, partial differential equations, nonlinear diffusion, and mathematical methods in image processing and analysis.

Huijun Gao received his PhD degree in control science and engineering from the Harbin Institute of Technology (HIT), Harbin, China, in 2005. From 2005 to 2007, he was a postdoctoral researcher with the Department of Electrical and Computer Engineering, University of Alberta, Edmonton, AB, Canada. Currently, he is a professor and the director of the Research Institute of Intelligent Control and Systems, HIT. His research interests include network-based control and time-delay systems.